THE ATACAMA COSMOLOGY TELESCOPE: THE RECEIVER AND INSTRUMENTATION

D. S. Swetz[1,2], P. A. R. Ade[3], M. Amiri[4], J. W. Appel[5], E. S. Battistelli[6,4], B. Burger[4], J. Chervenak[7],
M. J. Devlin[1], S. R. Dicker[1], W. B. Doriese[2], R. Dünner[8], T. Essinger-Hileman[5], R. P. Fisher[5], J. W. Fowler[5],
M. Halpern[4], M. Hasselfield[4], G. C. Hilton[2], A. D. Hincks[5], K. D. Irwin[2], N. Jarosik[5], M. Kaul[1], J. Klein[1],
J. M. Lau[9,10,5], M. Limon[11,1,5], T. A. Marriage[12], D. Marsden[1], K. Martocci[13,5], P. Mauskopf[3], H. Moseley[7],
C. B. Netterfield[14], M. D. Niemack[2,5], M. R. Nolta[15], L. A. Page[5], L. Parker[5], S. T. Staggs[5], O. Stryzak[5],
E. R. Switzer[13,5], R. Thornton[1,16], C. Tucker[3], E. Wollack[7], Y. Zhao[5]

Draft version July 5, 2010

ABSTRACT

The Atacama Cosmology Telescope was designed to measure small-scale anisotropies in the Cosmic Microwave Background and detect galaxy clusters through the Sunyaev-Zel'dovich effect. The instrument is located on Cerro Toco in the Atacama Desert, at an altitude of 5190 meters. A six-meter off-axis Gregorian telescope feeds a new type of cryogenic receiver, the Millimeter Bolometer Array Camera. The receiver features three 1000-element arrays of transition-edge sensor bolometers for observations at 148 GHz, 218 GHz, and 277 GHz. Each detector array is fed by free space mm-wave optics. Each frequency band has a field of view of approximately $22' \times 26'$. The telescope was commissioned in 2007 and has completed its third year of operations. We discuss the major components of the telescope, camera, and related systems, and summarize the instrument performance.

Subject headings: Microwave Telescopes, CMB Observations

1. INTRODUCTION

Measurements of the Cosmic Microwave Background (CMB) provide a wealth of information about the origin and evolution of the Universe. Current measurements of the angular power spectrum from tenths of a degree to all sky have provided estimates of cosmological paramters and have begun to quantify the big bang process (e.g., Komatsu et al. (2009), Brown et al. (2009), Chiang et al. (2009), Sievers et al. (2009)). Detailed measurements at arcminute scales are placing tighter constraints on the standard cosmological model and probe possible deviations. These higher resolution measurements also reveal secondary effects on CMB anisotropy, from, for example, the Sunyaev-Zel'dovich (SZ) effect and gravitational lensing, which are important for understanding structure formation.

We have built the Atacama Cosmology Telescope (ACT), a custom six-meter telescope, to address these scientific questions. ACT features a cryogenic receiver, the Millimeter Bolometer Array Camera (MBAC), that operates at three frequencies: 148 GHz, 218 GHz, and 277 GHz. Each frequency band is imaged by a 32×32 array of transition-edge sensor (TES) bolometers. The telescope was commissioned at its site in late 2007, at which time the 148 GHz channel was installed in MBAC. The remaining two frequencies were installed in June 2008. Since then the telescope and completed camera have collected approximately twelve months of data over two observing seasons.

This paper presents the instrument and complements a set of ACT papers presenting the first generation of experimental results. The paper is organized as follows. In Section 2 we discuss the optical design and structure characteristics, site location, and telescope operation. Section 3 details the design of the MBAC cryostat, cold optics, and detectors. Telescope control, data acquisition, merging, and related topics are discussed in Section 4. Finally, we present the image quality of the system in Section 5. Companion papers that detail the beams and scientific results are Hincks et al. (2009) and Fowler et al. (2010).

[1] Department of Physics and Astronomy, University of Pennsylvania, 209 South 33rd Street, Philadelphia, PA, USA 19104

[2] NIST Quantum Devices Group, 325 Broadway Mailcode 817.03, Boulder, CO, USA 80305

[3] School of Physics and Astronomy, Cardiff University, The Parade, Cardiff, Wales, UK CF24 3AA

[4] Department of Physics and Astronomy, University of British Columbia, Vancouver, BC, Canada V6T 1Z4

[5] Joseph Henry Laboratories of Physics, Jadwin Hall, Princeton University, Princeton, NJ, USA 08544

[6] Department of Physics, University of Rome "La Sapienza", Piazzale Aldo Moro 5, I-00185 Rome, Italy

[7] Code 553/665, NASA/Goddard Space Flight Center, Greenbelt, MD, USA 20771

[8] Departamento de Astronomía y Astrofísica, Facultad de Física, Pontificía Universidad Católica, Casilla 306, Santiago 22, Chile

[9] Kavli Institute for Particle Astrophysics and Cosmology, Stanford University, Stanford, CA, USA 94305-4085

[10] Department of Physics, Stanford University, Stanford, CA, USA 94305-4085

[11] Columbia Astrophysics Laboratory, 550 W. 120th St. Mail Code 5247, New York, NY USA 10027

[12] Department of Astrophysical Sciences, Peyton Hall, Princeton University, Princeton, NJ USA 08544

[13] Kavli Institute for Cosmological Physics, 5620 South Ellis Ave., Chicago, IL, USA 60637

[14] Department of Physics, University of Toronto, 60 St. George Street, Toronto, ON, Canada M5S 1A7

[15] Canadian Institute for Theoretical Astrophysics, University of Toronto, Toronto, ON, Canada M5S 3H8

[16] Department of Physics , West Chester University of Pennsylvania, West Chester, PA, USA 19383

2. THE ATACAMA COSMOLOGY TELESCOPE

2.1. *Telescope Construction and Optics*

The diameter of the six-meter primary reflector was set by the requirement to obtain arcminute-resolution at the ACT frequencies. The primary and two-meter secondary are arranged in an off-axis Gregorian configuration to give an unobstructed image of the sky. The primary focal length was fixed at 5.2 m. This results in a com-

pact arrangement between the primary and secondary reflectors, making it easier to achieve the fast scanning specifications of the telescope (Section 2.3). The design is described in Fowler et al. (2007). The telescope was built by Amec Dynamic Structures Ltd. (now Empire Dynamic Structures).

Figure 1 shows the major components of the telescope structure and Table 1 the important parameters. To minimize ground pick-up during scanning, the telescope has two ground screens. A large, stationary outer ground screen surrounds the telescope. A second, inner ground screen connects the open sides of the primary reflector to the secondary reflector, and moves with the telescope during scanning. A climate-controlled receiver cabin is situated underneath the primary and secondary reflectors. The telescope was designed to work with MBAC (Section 3), and also to be able to accommodate future receivers.

TABLE 1
PHYSICAL PROPERTIES OF THE TELESCOPE AND OPTICS

Telescope Properties		Location	
Telescope height	12 m	Altitude	5190 m
Ground screen height	13 m	Longitude	$67°47'15''$W
Total mass	52 t	Latitude	$22°57'31''$S
Moving structure mass	40 t	$\cdots$	$\cdots$
Optics			
f-number[a]	2.5	Azimuth range	$\pm220°$
FOV[a]	1 deg^2	Max. az speed	$2°$/s
Primary reflector Dia	6 m	Max. az acc.	$10°$/s^2
No. primary panels	71	Elev range	$30°.5 - 60°$
Secondary reflector Dia	2 m	Max. elev speed	$0.2°$/s
No. secondary panels	11	$\cdots$	$\cdots$

[a]At telescope Gregorian focus

Using the Gregorian design as a starting point, the reflector shapes were numerically optimized to increase the field of view over a classic Gregorian using Code V optical design software.[1] At the Gregorian focus before reimaging (Section 3.1), the telescope achieves a Strehl ratio greater than 0.9 over a 1 square-degree field at 277 GHz. Details of the numerical optimization and reflector formulae are given in Fowler et al. (2007). The telescope approaches an aplanatic system with no leading-order spherical aberrations or coma in the focal plane. Figure 2 shows a ray trace through the telescope-camera system. The fast focal ratio ($F = 2.5$) allows the MBAC window (Section 3.2) to be small.

To minimize the beam sizes and maximize the collecting area, 97% of the primary reflector diameter is illuminated, limited by a cold aperture stop (the "Lyot stop"). Spillover at the Lyot stop inside MBAC can load the detectors with radiation emitted from warm, nearby structures. Calculations show that there is a maximum of 0.5% spillover on the primary reflector and 2% spillover on the secondary reflector. To reduce this spillover loading, the primary reflector has a 0.75 m radial baffle that reduces the primary spillover to < 0.2%. However, the spillover on the secondary reflector occurs at larger angles. While there is a 0.3 m radial baffle around the

secondary, it does little to reduce the effective spillover. Measurements of the detectors indicate that there is as much as 2–3% spillover that does not get reflected to the cold sky. As a result, the secondary baffling is being redesigned to ensure that the majority of the spillover is redirected to the sky in future observations.

2.2. Site Location, Band Selection, and Logistics

The ACT site is at an altitude of 5190 m near the peak of Cerro Toco in the Atacama Desert of northern Chile. The telescope location provides visibility to approximately 70% of the sky. The high elevation and low precipitable water vapor (PWV) at this location provides excellent millimeter and submillimeter atmospheric transparency and has attracted several other millimeter-wave experiments. The specific ACT site has also been used by the TOCO (Miller et al. 2003) and Millimeter INTerferometer (Fowler et al. 2005) telescopes.

The ACT bands were selected to discriminate between the SZ, CMB, and point sources. The bands were also chosen to avoid three large emission features, an oxygen emission line at 119 GHz and water emission lines at 183 GHz and 325 GHz (e.g, Danese and Partrige (1989)). Using the National Radio Astronomy Observatory/European Southern Observatory monitoring data and an atmospheric modeling program developed by Pardo et al. (2001), the opacity and Raleigh-Jeans (RJ) brightness temperatures are extrapolated to the ACT bands. The level of emission in the continuum where the ACT bands lie is due to O_2 and H_2O in comparable parts. Thus, the transmission and absorption in the bands is a function of the PWV in the atmosphere. Seasonal changes in the weather provide sustained periods with low amounts of water vapor and naturally set the ACT observing season to April through December when the PWV is lowest due to the colder weather.

The ACT site is approximately 50 km from the town of San Pedro de Atacama (altitude ~ 2750 m), the location of lodging and the main field office. Travel to the site from North America takes approximately one day. The roads are clear year-round with brief periods of inaccessibility due to snow, providing site access throughout the year. Communication with the site is possible through a data link consisting of a 60 cm parabolic antenna in San Pedro and a 1.2 m parabolic antenna at the site, and an Orthogon PTP600 transreceiver pair operating at 5.8 GHz.[2] The overall communications rate is ~ 40 Mb/s. Connection to the Internet is made in San Pedro; this connection limits the speed of communication from North America and the site to 1–2 Mb/s.

Site electricity is alternately supplied by one of two XJ150 John Deere (Triton Power Generation) diesel generators, with sufficient on-site fuel for 60 days of autonomous operation at ~ 240 liters per day. The generators are rated at 150 kW (at sea level), but typical consumption during full operation is approximately 25–30 kW.

2.3. Scan Strategy

The sky is scanned to separate the CMB signal from drifts in the detectors and atmosphere. Often, this

---

[1] Business address: Optical Research Associates, 3280 East Foothill Blvd., Pasadena, CA, 91107. Internet URL: http://www.opticalres.com/.

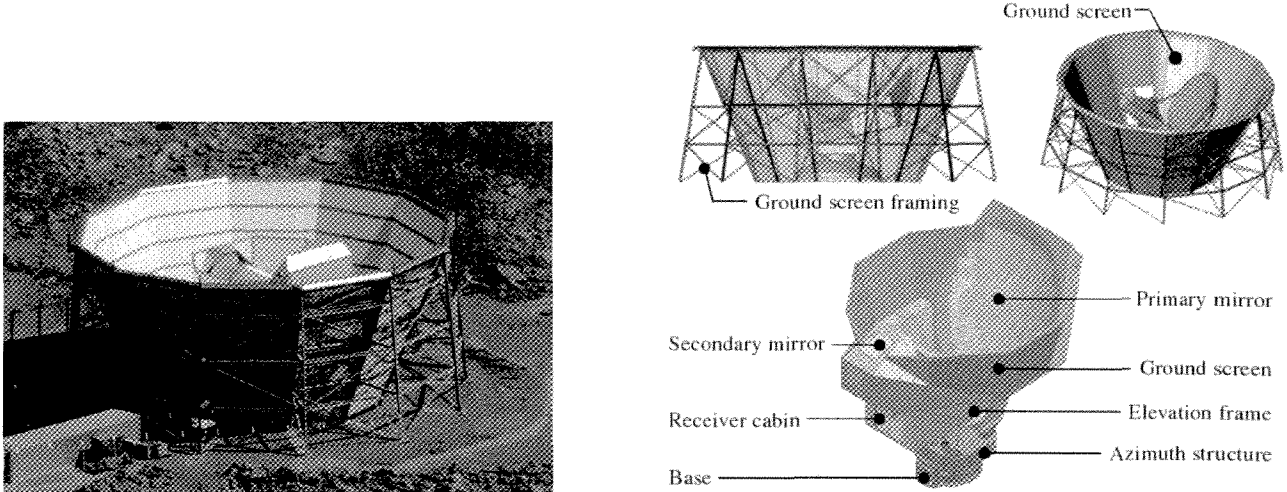[2] Orthogon is a subsidiary of Motorola. For more information see www.motorla.com.

FIG. 1.— Picture *(left)* and mechanical rendering *(right)* of ACT and its ground screens. The telescope has a low profile; the full height is 12 m. The entire upper structure ("Azimuth structure" and above) rotates as a unit. The surrounding outer ground screen shields the telescope from ground emission. The screen also acts as a wind shield. An inner ground screen mounted on the telescope connects the sides of the secondary and primary. The primary reflector is 6 m and is surrounded by a 0.5 m guard ring (Figures courtesy of AMEC Dynamic Structures).

is done by moving the telescope beam on the sky on timescales faster than the $1/f$ knee of the low frequency noise but slower than the time constants of the detectors. For ACT, the entire 40 metric-ton upper structure typically scans at $1°5/s$ in azimuth while holding the elevation fixed (typically at $50°5$). Scans are done at two positions, east and west of an arc between the south celestial pole (SCP) and the zenith. As the sky rotates, an annulus around the SCP is mapped out.

This strategy has several benefits for observations from the ground. Changing the amount of airmass affects both the gain of the system due to atmospheric absorbtion and the background loading from gray body emission. Keeping the elevation fixed ensures the amount of atmospheric airmass is relatively constant during a scan, preventing a scan-synchronous atmospheric signal. Second, by performing scans both east and west along the SCP-zenith arc, the mapped annulus will be observed in two different cross-linked orientations. Cross-linking has been shown to be important for the removal of scanning-induced systematic effects such as striping when making maximum likelihood maps (Wright 1996; Tegmark 1997) of the millimeter sky. Finally, by moving the entire upper structure of the telescope, including the primary, secondary, and receiver, the detectors are constantly looking through the same optics. This avoids any scan-synchronous signals such as beam shape, reflector emission, or ground pick-up that could potentially arise from changing the optical path.

2.4. Pointing

The typical telescope scan has an amplitude between 5 and 7 degrees with constant velocity between turnarounds, when the telescope changes direction at the end of a scan. Rapid turnarounds at the end points of the scan minimize time spent not scanning, which maximizes the sky overlap of the three separate arrays as discussed in Section 3.1 (see Figure 5). The telescope is designed to produce a maximum scan speed of $2°/s$ with a turnaround time of less than $400\,ms$ $(10°/s^2)$ while maintaining a pointing error of $6''$ rms from the commanded position in both azimuth and elevation. The rapid turnarounds combined with the 40 metric-ton scanning component of the telescope made the pointing stability during scanning a considerable challenge.

The telescope motion systems were designed by KUKA, a robotics systems company.[3] The KUKA robot comprises the motor drivers, an uninterruptible power supply, an embedded computer with a solid-state drive, and operator console. The KUKA robot monitors the telescope position using a pair of Heidenhain absolute encoders (27-bit, $0.0097''$ accuracy) on the azimuth and elevation axes. For down-stream pointing reconstruction, a second set of identical encoders is read out synchronously with the $\approx 400\,Hz$ bolometer data stream. A DeviceNet network relays telescope motion parameters between the KUKA robot controller and a housekeeping computer (Section 4.3).[4] KUKA's robot also produces a stream of telescope health information (its internal encoder and resolver readouts, motor currents and temperature) which are broadcast via the user datagram protocol (UDP) and recorded by the housekeeping computer at 50 Hz. Inclinometers are mounted on the telescope base and the rotating structure to measure tilt, and accelerometers are mounted at four positions along the center of the primary reflector and one near the secondary reflector. The readout of these devices is synchronized to within $5\,\mu s$ of the detector data (Switzer et al. 2008). The elevation encoder readings are well within the pointing requirements during the constant-velocity portion of the scan.

During science observations, the scan speed is $1°5/s$. The acceleration at turnaround is reduced so that it takes 800 ms to change direction. With these parameters, the telescope stays within $2''$ rms of the desired path the entire time, and the sky is observed through the entire scan.
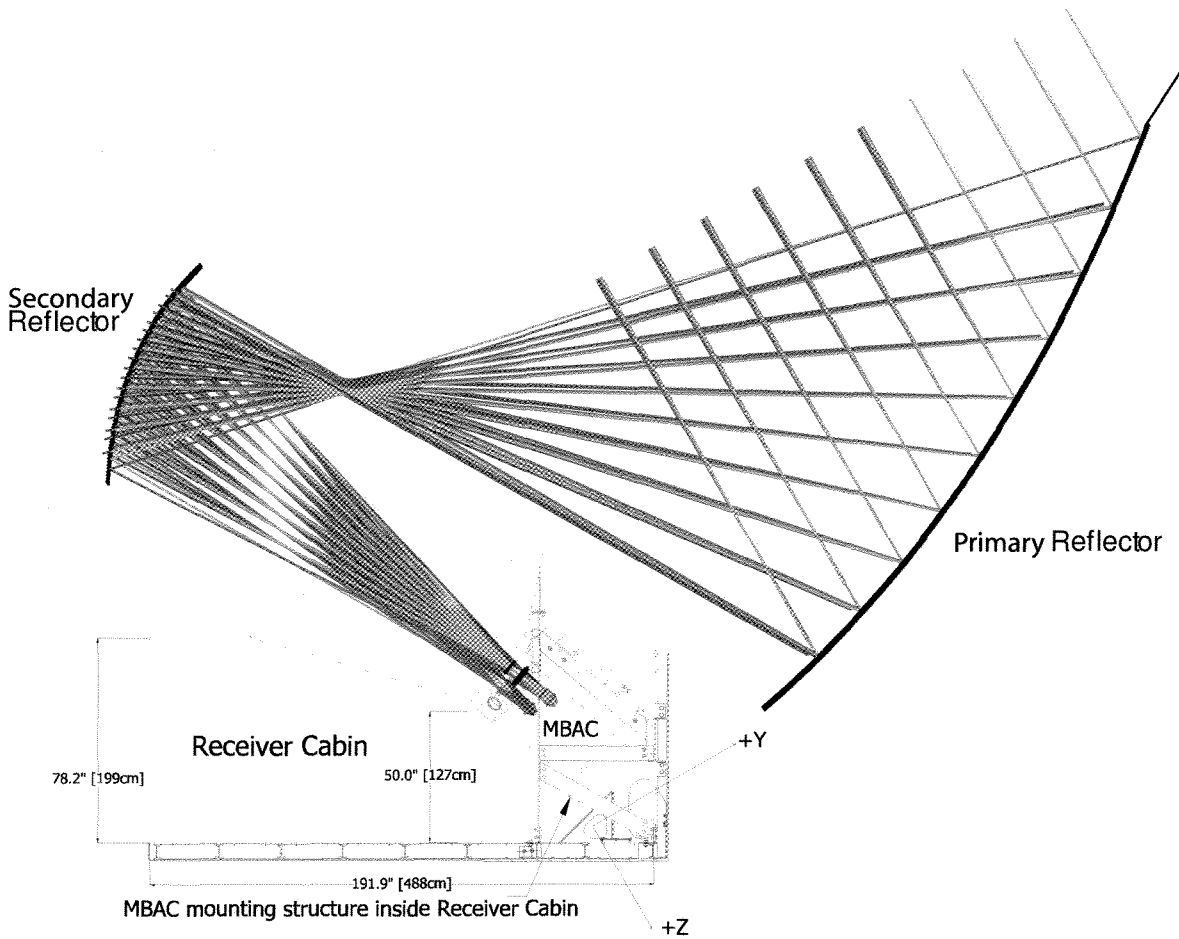
2.5. Reflector Alignment

FIG. 2.— Ray trace of ACT's primary and secondary reflectors. The telescope is an off-axis numerically optimized Gregorian. The rays are traced into the MBAC cryostat, mounted on the far right of the receiver cabin. The service position (position where the receiver-cabin floor is level) is shown, corresponding to a viewing elevation of 60°. The nominal observing elevation is 50°.5. The rays are traced for the highest (blue), central (green), and lowest (red) fields in both the 277 GHz camera (higher in the cryostat) and the 218 GHz camera (lower in the cryostat). The Figure also shows the dimensions and location of the receiver cabin and MBAC mounting structure.

The telescope's six-meter primary and two-meter secondary reflectors are composed of individually machined aluminum panels mounted to a back-up structure (BUS). The primary consists of 71 roughly rectangular panels laid out in eight rows. The panels comprising each row are identical, but the curvature of the panels decreases with increasing height of the BUS (Figure 3). An individual panel measures $\approx 0.65 \times 0.85$ m and weighs 10 kg. The secondary reflector is assembled by arranging 10 trapezoidal panels, measuring $\approx 0.35 \times 0.80$ m, around a $\approx 0.50 \times 0.80$ m decagonal-shaped central panel. The panels, manufactured by Forcier Machine Design, were individually machined to their required surface shape.[5] They were measured using a coordinate-measuring machine (CMM) to have an rms deviation from the expected shape of ≈ 3 μm.

The backside of each panel of the primary and secondary reflector is attached to the telescope structure near the four corners of the panel, and is thus over-

constrained. Threaded mechanisms at these attachment points allows for manual coarse and fine adjustment of the position of each panel (Woody et al. 2008).

The loss in forward gain due to panel-to-panel misalignment was estimated with the Ruze formula (Ruze 1966). To achieve $\approx 90\%$ of the optimal forward gain at our highest frequency of 277 GHz, a surface rms of 27 μm is required assuming a Gaussian distribution of phase errors. The panel positions are measured using a laser tracker manufactured by Faro.[6] The tracker measures the time of flight of a laser pulse to determine the distance to a point on the reflector's surface. Corner cubes and retroreflectors are used on every panel to measure alignment. After three years and six sets of measurements of the primary, the rms has consistently been in the 25-30 μm range, and 10-12 μm for the secondary. Figure 3 shows the alignment results obtained prior to the 2009 observing season.

After the individual panels have been set, the position of the secondary can be adjusted as a unit using linear

[5] Business address: 123 Marshall Ave, Petaluma, CA 04052, USA.

[6] Internet URL: http://www.faro.com.

-100   0   100
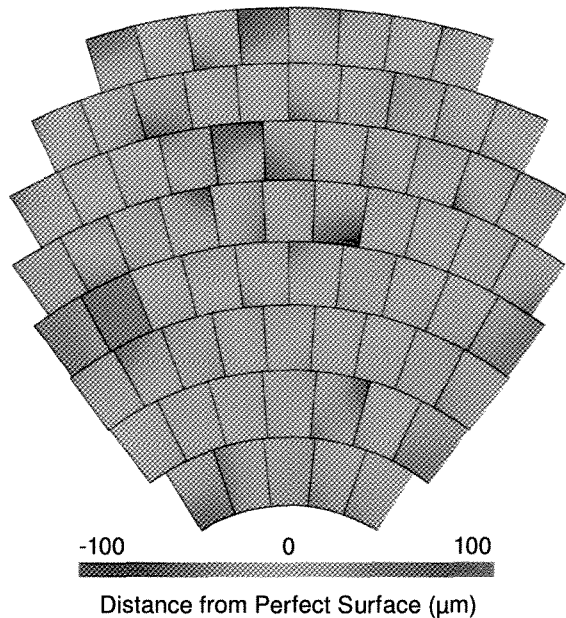
Distance from Perfect Surface (μm)

FIG. 3.— Primary reflector layout and final reflector alignment. The primary is composed of 71 approximately rectangular panels arranged in eight rows. The panels are attached to the telescope BUS and are aligned using four adjustment screws on the panel back-side. Panel positions are measured using a laser tracker. The residuals of a fit to the reflector's equation give the necessary adjustments. The figure shows the residual after the final adjustments for the 2008 observing season were made. The reflector was aligned to better than 30 μm rms.

actuators mounted on the secondary frame. This can be performed remotely by the telescope control software. The adjusters allow ±1 cm motion in y and z, and rotations of ±1° in azimuth and elevation. Optimal focus is achieved by analyzing the detector response to planets at various positions for the secondary.

3. THE MILLIMETER BOLOMETER ARRAY CAMERA

MBAC is a cryogenic camera designed specifically to meet the scientific goals of the ACT project. The design entails three independent sets of cold reimaging optics, one for each frequency. Achieving the sensitivity goals of the project requires that the detectors operate at 300 mK.

3.1. *Cold Reimaging Optics*

The Gregorian telescope produces large field of view suitable for a several square degree camera. Three sets of cold optics reimage parts of this field onto three separate focal plane arrays (Figure 4). Due to the off-axis Gregorian design, the optimal focal plane is not perpendicular to the optical axis. Due to the non-telentric, off-axis design, the cold optics are held at compound angles inside the cryostat. The specifications required a diffraction-limited field of view for each 22' × 26' array. Each set of reimaging optics has a cold aperture stop that defines the illumination of the secondary and primary reflectors.

The three optics tube design has several advantages. Wide-band anti-reflective (AR) coatings can be difficult to produce, optimizing over a small band leads to higher transmission through the optical elements. The optical components at a given frequency are on-axis and cylin-

drically symmetric. This geometry allows the optical elements to be placed in an optics tube that provides shielding for the arrays against stray radiation, and leads to a simpler mechanical design. Each optics tube was built separately, allowing for greater flexibility. Several aspects of the camera design were based on the MUSTANG instrument on the Green Bank Telescope (Dicker et al. 2008) and on the prototype instrument for ACT, CCAM (Lau 2008; Aboobaker 2006).

A disadvantage of the design is that the three arrays do not image the same region of sky simultaneously. The offset between arrays is minimized by packing them as closely together as mechanically possible. The resulting triangular configuration places the 277 GHz camera in the plane of symmetry of the telescope due to its tighter diffraction requirements, and the 148 and 218 GHz cameras below and on either side of the plane of symmetry. This arrangement coupled with the ACT scan strategy maximizes the total sky coverage overlap among the different frequencies. As the telescope scans back and forth, most of the scanned area is covered by both of the bottom two arrays; only in the turnaround regions, chosen to be short in duration, are the two fields not overlapping. Sky rotation moves the lower observed region through the upper camera when observing in the east (or vice-versa when the telescope is observing in the west).

All the lenses are made out of high-purity silicon, chosen for its high index of refraction ($n = 3.416$) (Lamb 1996) and high thermal conductivity at cryogenic temperatures. High-purity was used to reduce absorption loss at millimeter wavelengths. An AR layer is added to each lens by coating it on both sides with a thin layer ($\approx$ several hundred μm, the exact number depending on the frequency) of machined Cirlex ($n = 1.84$) (Lau et al. 2006). The first lens, located just after the Gregorian focus, forms an image of the primary mirror on the cold aperture stop. Bare arrays, such as those used in MBAC, accept radiation from all directions. Illumination is controlled using a cold (1 K) Lyot stop located after the first lens. Since the cold stop is not a perfect image of the primary, individual detectors geometrically illuminate approximately 5.6 m of the primary reflector.

The second and third lenses refocus the sky onto the focal plane arrays. The optics were designed to maximize the Strehl ratio over the focal plane. The placement of the final lens with respect to the array has the tightest tolerance of all optical elements, ≈ 600 μm.[7] Hence the final lens and array were designed as a single mechanical unit at 300 mK. The final band-pass filter sits in front of the final lens and is also cooled to ≈ 300 mK (Fig 4).

The detectors are 1.050 × 1.050 mm squares, with a spacing of 1.050 ± 0.002 mm (horizontal) by 1.22 ± 0.02 mm (vertical). The horizontal error is based on fabrication estimates and the vertical error is based on machine tolerance. This results in the 32 × 32 rectangular detector grid measuring approximately 33.6 ± 0.1 × 39.0 ± 0.1 mm, where the errors are estimates from assembly and machining tolerances. Table 2 summarizes their physical and optical properties. The numbers for the focal length, primary illumination, and focal ratio vary across the array. The numbers reported in Table

---

[7] The tolerance criteria was defined as the amount a lens needed to be misplaced to produce a 1% decrease in the Strehl ratio.
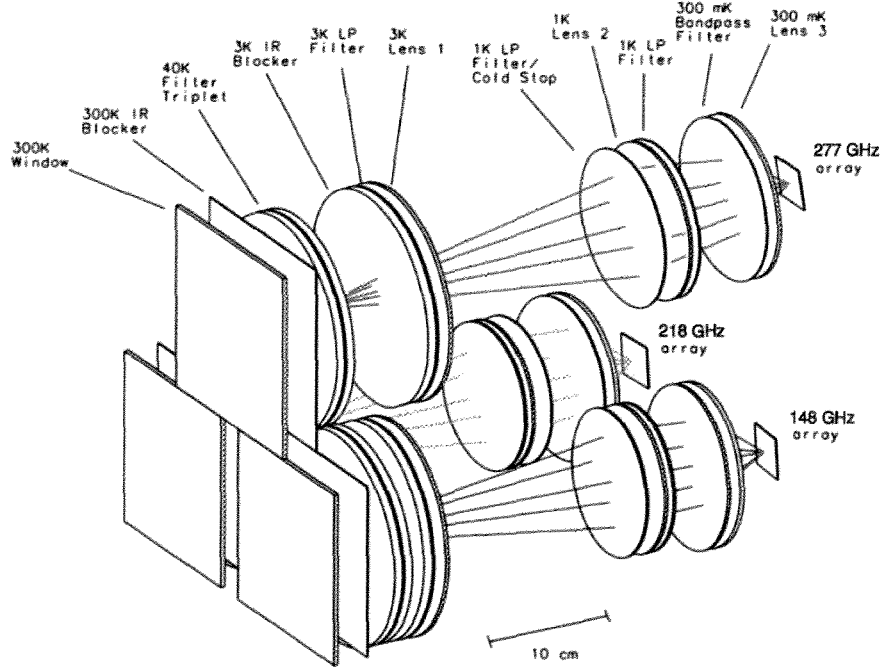
FIG. 4.— Three dimensional model of the cold reimaging optics for MBAC. The optical elements for each array are separated into individual optics tubes. Each array has a similar set of optical elements. The 277 GHz elements and temperatures are labeled. The lenses are labeled Lens 1 to 3, with Lens 1 one being closest to the 300 K window. The low-pass capacitive-mesh filters are labeled LP and the band-pass filter as BP. Infrared blocking filters are labeled IR. The temperature of the components decreases moving toward the arrays to reduce the loading, with the band-pass filter, the third lens, and arrays all held at 0.3 K.

2 are calculated from a model and the "uncertainties" are the maximum and minimum range. The field of view is $\approx 22' \times 26'$ for each array. In terms of angle on the sky, the detectors are spaced approximately $1/2F\lambda$ to $1.1F\lambda$ going from the lowest to highest frequencies. This means that for 148 GHz, the entire field is fully sampled in a single pointing. There are no feed horns in the system. Figure 5 shows the the relative sky spacing of the detectors for the three arrays.

Calculations using optics design software predict Strehl ratios greater than 0.97, 0.94, and 0.96 across the entire focal plane region, with average Strehl ratios of 0.99, 0.98 and 0.98 for the 148, 218, and 277 GHz cameras, respectively.

3.2. Vacuum Windows

The vacuum window location was chosen near the Gregorian focus of the telescope to minimize the window size, which in turn reduces the load on the cryogenic stages. A separate window was used for each of the three frequencies, each with an optimized AR coating. The close spacing of the optics dictated a rectangular window shape, which takes advantage of the image shape of the array at the window. The vacuum windows are made of 4 mm-thick Ultra High Molecular Weight Polyethylene (UHMWPE) with an index of refraction of ~ 1.53 at 160 GHz (Lamb 1996). The AR coatings consist of bonded expanded-Teflon sheets glued to the front and back surfaces of the UHWPE. Measurements of the MBAC windows using a Fourier transform spectrometer (FTS) show transmissions of over 96% for the 148 GHz

TABLE 2
DETECTOR ARRAY PHYSICAL AND OPTICAL PROPERTIES

Detector Physical Properties		
$\cdots$	Horizontal	Vertical
Pixel size	1.050 mm	1.050 mm
Pixel spacing[a]	1.050±0.002 mm	1.22±0.02 mm
Array configuration	32	32
Array size[b]	33.6±0.1 mm	39.0±0.1 mm
Optical Properties: 148 and 218 GHz Arrays		
$\cdots$	Horizontal	Vertical
Effective focal length[c]	5.17±0.12 m	5.03±0.13 m
Primary illumination[c]	5.60±0.21 m	5.59±0.23 m
Focal ratio[c]	0.93±0.02	0.90±0.02
Detector spacing	41±4″	50±4″
Optical Properties: 277 GHz Array		
$\cdots$	Horizontal	Vertical
Effective focal length[c]	5.41±0.11 m	5.06±0.12 m
Primary illumination[c]	5.48±0.19 m	5.50±0.20 m
Focal ratio[c]	0.98±0.04	0.91±0.04
Detector spacing	40±4″	49±4″

[a]Horizontal error estimated from fabrication tolerances. Vertical error estimated from machining tolerances.
[b]Errors are estimated from machining and assembly tolerances.
[c]The number varies across the array and the "±" indicates the maximum and minimum of the range.

and 218 GHz bands and over 93% in the 277 GHz band (Swetz 2009).

3.3. Filters and Bandpass Measurements

The frequency responses of the bolometric detector arrays for MBAC are defined by the transmission through the optical elements in the optical path to the detec-

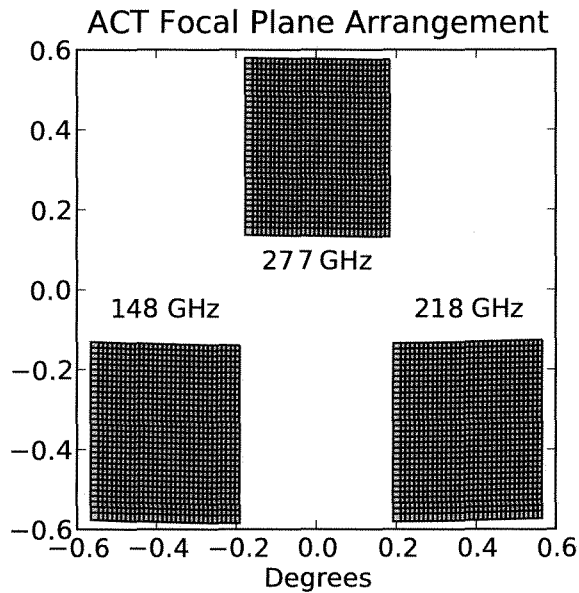## ACT Focal Plane Arrangement

FIG. 5.— The idealized arrangement of the ACT detectors on the sky. This arrangement on the sky is the reverse of the view when looking into MBAC (Fig. 4).

tors. The frequency transmission band is set primarily by a series of low-pass (LP) capacitive-mesh filters and a band-defining edge (BP) filter (Ade et al. 2006). Multiple filters are used because the LP filters have transmission leaks at harmonics of their cut-off frequency. The use of filters with a range of cut-off frequencies allows subsequent filters to suppress the out of band leaks from previous filters. Filters are placed at each successive cryogenic stage along the optical path to limit loading on the next stage. They are arranged from highest frequency cut-off to lowest. There are also a series of 4 μm thick infrared-blocking (IR) reflective filters to reduce the optical loading on the cold stages (Tucker and Ade 2006). These IR blocking filters prevent the center of the poorly conducting LP filters from heating up and consequently reduce the radiative loading from the windows. Each optics tube contains 10 filter elements, including the windows. Table 3 lists the nominal temperature, location, and low-pass cut-off frequency for each of the filters. Figure 4 shows all the filter and lenses in free space.

Each filter's frequency response at room temperature was measured using a FTS. A composite transmission spectrum was created by multiplying together the individually measured filter responses. After the filters were installed into MBAC, FTS measurements were made in the lab prior to shipping to Chile with a different spectrometer on the fully cooled system. It should be noted that at this time there was one additional element placed in the optical chain, an anti-reflective (AR) layer, directly in front of the detectors.

Using the instrument passband (normalized by the peak in the composite passband), we follow the method of Page et al. (2003) for calculating the effective central frequency of broadband sources, including the CMB and SZ effect. The effect of these sources on the band center is to shift it slightly. The results are given in Table 4.

TABLE 3
FILTER LOCATION, TEMPERATURE, AND CUT-OFF FREQUENCY OF THE FILTERS IN THE ORDER THEY ARE PLACED IN THE OPTICAL PATH.

Filter Type	Temperature	Frequency (GHz)		
		148	218	277
Window	Ambient	$\cdots$	$\cdots$	$\cdots$
IR blocker	Ambient	$\cdots$	$\cdots$	$\cdots$
IR blocker	40 K	$\cdots$	$\cdots$	$\cdots$
Low-pass[a]	40 K	360	360	540
IR blocker	40 K	$\cdots$	$\cdots$	$\cdots$
IR blocker	4 K	$\cdots$	$\cdots$	$\cdots$
Low-pass[a]	4 K	270	330	450
Low-pass[a]	1 K	210	300	390
Low-pass[a]	1 K	186	255	360
Band-pass[b]	300 mK	148	220	280

[a]Approximate frequency cut-off listed.
[b]Expected band center listed.

TABLE 4
PROPERTIES OF THE MBAC FILTERS.

Array	148 (GHz)	218 (GHz)	277 (GHz)
Comp. Bandcenter[a]	146.9	217.3	273.5
Max. Transmission[a]	0.74	0.72	0.69
Bandcenter[b]	149.2±3.5	219.7±3.5	277.4±3.5
Bandwidth[b]	18.4	17.0	20.9
Noise Bandwidth[b]	27.6	25.9	34.8
Band FWHM[b]	27.0	22.2	30.3
Effective Bandcenters[c]			
Synchrotron[c]	147.6	217.6	274.8
Free-free[c]	147.9	218.0	275.4
Rayleigh-Jeans[c]	149.0	219.1	276.7
Dusty source[c]	149.7	219.6	277.4
CMB[c]	148.4	218.3	274.7
SZ effect[c]	146.9	220.2	277.2
Conversion factors			
$\delta T_{CMB}/\delta T_{RJ}$	1.71±0.04	3.02±0.10	5.44±0.20
$\delta W/\delta T_{RJ}$ (pW/K)	0.569±0.055	0.483±0.055	0.699±0.055
Γ (μK/Jy)	6826±350	5824±240	4373±550

[a]Based on a composite of room temperature measurements. The source spectrum has been divided out. The effect of the lenses and coupling to the detectors is not included.
[b]Measurements were made with all filters installed in MBAC along with the lenses and the ACT detectors. This measurement includes neutral density filters in each band and the coupling of the FTS to MBAC. The neutral density filters are not present when observing the sky. Three measures of the width of the band are given. The uncertainties are obtained from a combination of the rms of the measurements and an estimate of the systematic error. The source spectrum has been divided out of the measured response.
[c]Effective band centers for synchrotron emission ($\alpha = -0.7$), free-free emission ($\alpha = -0.1$), Rayleigh-Jeans emission ($\alpha = 2.0$), dusty source emission ($\alpha = 3.5$). These values are based on the average of the computed composite of all filters and the measured response in MBAC. The uncertainty on all values is 3.5 GHz. For example, for the response to the CMB we use 148 GHz, 218 GHz in AR1 and AR2. Since the CMB will be difficult to detect in AR3 we use the RJ band center of 277 GHz.

3.4. Detectors

MBAC has three 1024-element (32 × 32) detector arrays, one for each frequency. The focal plane is filled by a tiling of free-standing bolometric sensors with square absorbers. The array elements are pop-up TES bolometers (Benford et al. 2003; Li et al. 1999), fabricated in the Detector Development Lab at NASA Goddard Space Flight Center. Each 20 mΩ TES is voltage-biased with

a $1\,\mathrm{m}\Omega$ shunt resistor. Each sensor array is enclosed in a cooled enclosure and its field of view of the incident radiation is limited by the cold stop.

The bolometers are fabricated in columns of 32 elements on silicon on insulator (SOI) wafers. These wafers have a 1.45 µm-thick silicon membrane separated by a thin layer of oxide from the 450µm bulk silicon. Each bolometer is a superconducting MoAu bilayer with $T_c \approx 500\,\mathrm{mK}$ atop a 1.05 mm × 1.05 mm square of the silicon membrane. The rest of the square is implanted with phosphorus ions that serve as the absorber, with a surface impedance of $\approx 100\,\Omega/\square$. The absorber is coupled to the bulk silicon by four 1 mm-long legs etched from the silicon membrane with widths between 5-20 µm, depending on the array. Two of the legs carry superconducting bias wiring for the TES. These legs define the thermal conductance G to the thermal bath, and are mechanically compliant enough so that each can be folded 90° so that the square absorbers are orthogonal to the planes of bulk silicon. The bulk silicon is then wire bonded to a silicon circuit board with superconducting (aluminum) wiring which exits the circuit board on superconducting (tin plated on copper) flexible circuits via zero insertion force (ZIF) connectors. These column assemblies are stacked to form the 32 × 32 array of detectors.

The sensitivities of the 148 GHz and 218 GHz arrays were $\approx 30\,\mu\mathrm{K}\,\mathrm{s}^{1/2}$ and $40\,\mu\mathrm{K}\,\mathrm{s}^{1/2}$, respectively in 2008, in CMB temperature units. These include atmospheric effects. Table 5 lists some of the basic properties of the TES detectors with their measured standard deviations for each of the three arrays, including their thermal conductivities, G, their critical temperatures, T_c, their dark noise (NEP), and their time constants, τ. For a more complete description of the ACT detectors, see Marriage et al. (2006); Niemack et al. (2008); Zhao et al. (2008).

TABLE 5
DETECTOR PARAMETERS

Array	G (pW/K)	T_c (mK)	Dark Noise (W / $\sqrt{\mathrm{Hz}}$)	τ (ms)
148 GHz	80 ± 20	510 ± 20	$(6 \pm 2) \times 10^{-17}$	1.9 ± 0.2
218 GHz	120 ± 30	510 ± 20	$(5 \pm 1) \times 10^{-17}$	2.5 ± 0.4
277 GHz	300 ± 60	500 ± 30	$(7 \pm 1) \times 10^{-17}$	1.6 ± 0.3

3.5. Detector Readout and Control

The individual bolometers are read out in a time-multiplexed fashion using Superconducting Quantum Interference Device (SQUID) multiplexers (Chervenak et al. 1999). Prior to exiting the cryostat, the bolometer signals are amplified by an array of approximately 100 SQUIDS in series held at 4 K. The series array amplifiers and multiplexers are controlled and read out by the Multi-Channel Electronics (MCE) (Battistelli et al. 2008).

Each of the three bands has an independent MCE which is mounted directly onto the MBAC cryostat. The MCEs, their power supplies, and MBAC all reside in the telescope receiver cabin. The three MCEs are connected to three storage and control computers in the equipment room through multimode fiber-optic carriers. The signals

from each MCE are decoded by a PCI card from Astronomical Research Cameras, Inc. in each of the three data acquisition computers.[8]

The base clock rate of the MCE is 50 MHz. This is divided down to 100 clock cycles per detector row by 32 detector rows plus one row of dark SQUIDs. Thus, the native read-rate of the array is 15.15 kHz as it leaves the cryostat. Nyquist inductors at 0.3 K band-limit the response so the array can be multiplexed with minimal aliased noise while maintaining stability of the loop (Niemack et al. 2008; Niemack 2008). To downsample the 15.15 kHz multiplexing rate to 399 Hz, the MCE applies a 4-pole Butterworth filter with a rolloff $f_{3\mathrm{dB}} = 122$ Hz to the feedback stream from each detector. This filter is efficient to implement digitally and has a flat passband. The downsampling to 399 Hz, which can be obtained by pulling every 38th sample (at 15.15 kHz) from the filter stack, is synchronized by similar clock counting in the synchronization box. Each time an MCE receives a system trigger, it packages the output of the $32 \times 32 + 1 \times 32$ (32 dark SQUIDs) array and sends it over a fiber optic to a PCI card on its acquisition computer in the equipement room, where it is buffered and written to disk. Additional information that fully specifies the MCE state in each 10-minute acquisition interval is written to a text "run file."

3.6. Magnetic Shielding

The SQUID multiplexers and amplifiers are sensitive to changing magnetic fields. They require magnetic shielding from both Earth's DC field and AC fields induced by the telescope motion through Earth's DC field and potential fields such as those generated from the telescope motors. The series array amplifiers are located outside of the optics tubes and are self-contained units enclosed within their own magnetic shielding. The SQUID multiplexers, however, are mounted on the silicon cards that make up each column in the detector array holder.

Because of their proximity to the array it would be difficult to provide individual magnetic shielding. The effectiveness of the magnetic shielding is highly dependent on the shield geometry. Given the details of geometry of the detector arrays in the optics tube, it was found that the best solution was to enclose each optics tube in magnetic shielding.

Cryoperm-10 is an alloy with a high nickel concentration.[9] Its composition coupled with a proprietary heat treatment give it a high magnetic permeability at cryogenic temperatures. To achieve the maximum attenuation, our shielding uses the thickest available Cryoperm, 1.5 mm. We also use multiple layers (Figure 6) which, given sufficient spacing between them, approaches the limit of multiplicative increases in the field attenuation.

Each layer of shielding has different dimensions, ports, and tubulations, making it difficult to calculate the magnetic field attenuation at the SQUIDs analytically. Computer simulations using Maxwell were employed to ap-
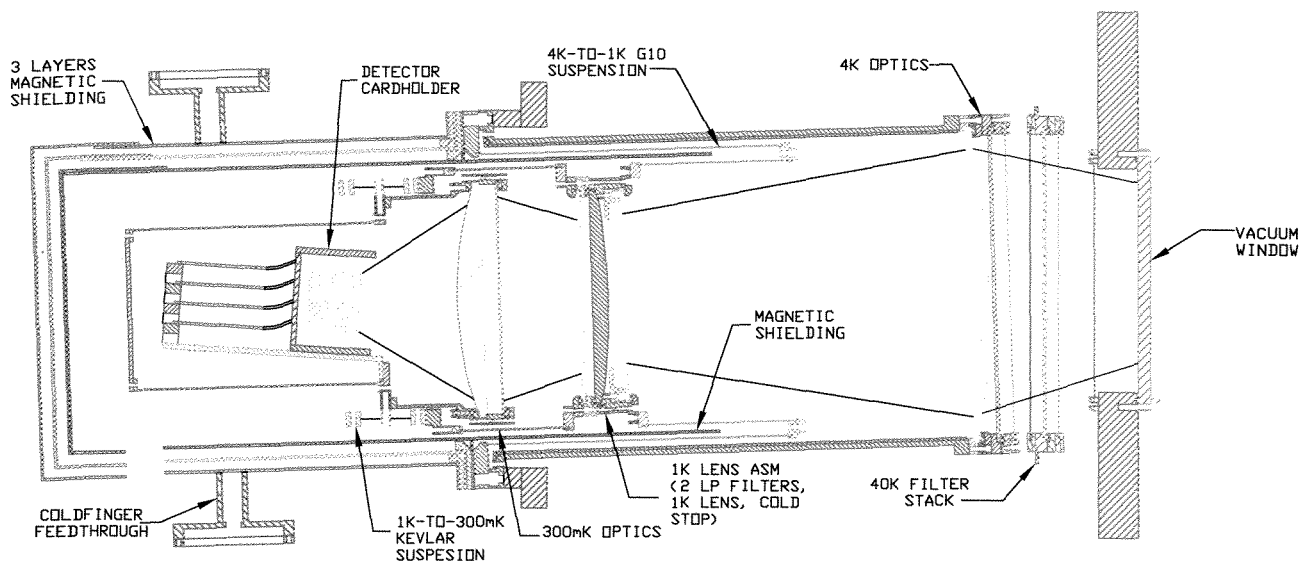
FIG. 6.— Cross section of the 148 GHz optics tube. Elements at five different temperatures, and the structures that separate them, are visible. Multiple layers of magnetic shielding are used wherever possible, including three layers around the detector cavity.

ply AC fields to the geometry of our shields.[10] These simulations estimate the attenuation to be nearly 40 dB (Thornton et al. 2008).

3.7. *Cryogenics*

The cryogenic design was dictated by a number of requirements. The site location makes the use of non-recycled liquid cryogens difficult and expensive; the optics design requires multiple stages of cooling to reduce detector loading; the three detector arrays need to be maintained at 300 mK continuously for over 12 hours, and the system must recycle in < 12 hours; the cryogenics must be stable when the telescope is scanning.[11] In order to meet these requirements, MBAC incorporates three different cooling mechanisms. A schematic of the thermal connections in the cryostat is shown in Figure 7.

The first stage and primary cooling stage is achieved using two pulse tube cryocoolers.[12] The first stage of the pulse tubes cool the 40 K components (Figure 7). The second stage of each pulse tube cooler (4 K) is connected to the condenser plate of one of the two custom ^{4}He sorption refrigerators. The refrigerators have base temperatures of ≈ 700 mK.

The motivation behind two ^{4}He refrigators was to use one "optics" refrigerator to cool all 1 K optical components, and one "backing" refrigerator to precool the ^{3}He refrigerator, the final cooling stage, capable of reaching 250 mK. However, to maximize the hold time of the system, the cooling of the 280 GHz 1 K optics was switched to the ^{4}He "backing" refrigerator after the first observing season. At the coldest stage, the evaporator of the ^{3}He refrigerator cools the 0.3 K lenses, filters, and detec-

tor arrays. For more details on the design of the sorption refrigerators, see Devlin et al. (2004) and Lau et al. (2006). The ^{4}He sorption refrigerators were measured to have 80 Joules cooling capacity and the ^{3}He refrigerator was measured to have 5.8 Joules cooling capacity.

The recycling procedure is completely automated and can be controlled remotely. The total recycle time for all three sorption refrigerators is ~ 6 hours. The detector are thermally regulated to 313 mK, slightly above the base temperature of the refrigerator, to reduce the effects of mechanical heating due to the motion of the telescope. This is done with independent servos on each array.

The pulse tube pulses at a frequency of 1.4 Hz, resulting in an intrinsic 100 mK temperature variation at 4 K and an attendant mechanical vibration. Careful selection of thermal connections and masses prevented thermal oscillations associated with the pulse tube being detected at either the 1 K stage or 300 mK stage. Mechanical coupling at the pulse frequency is mitigated by using a compliant acoustically deadened braided copper rope to attach the pulse-tube cryocoolers to the cryogenic stages.

The pulse-tube coolers operate at maximum capacity only when they are near vertical. Therefore the refrigerators are mounted so that they are vertical when the telescope is pointed at 45° in elevation, near the middle of its range. Since the telescope also looks at planets for calibration and pointing reconstruction, cryogenic tests have been performed with MBAC at both 60° and 30°. At these angles, there is little reduction in performance. A comprehensive description of the cryogenics is given in Swetz et al. (2008).

3.8. *Cryostat Mechanical Design*

The vacuum shell is a cylinder measuring 0.94 meters in diameter and 1.22 meters long made out of 6.35 mm (0.25 inch) thick aluminum. The shell diameter was dictated by the area of the focal plane, and the length by the focal length of the reimaging cold optics. A cut-away illustrating the major internal components is shown in Figure 8. The front plate of the shell is 25.4 mm (1 inch)

---

[10] Maxwell is a product of Ansoft. Internet URL: http://www.ansoft.com.

[11] The ACT observes from sunset to sunrise; daytime observations are not possible because solar heating of the telescope causes deformation of the telescope structure significantly increasing the $\approx 30~\mu$m rms of the primary mirror (Hincks et al. 2008).

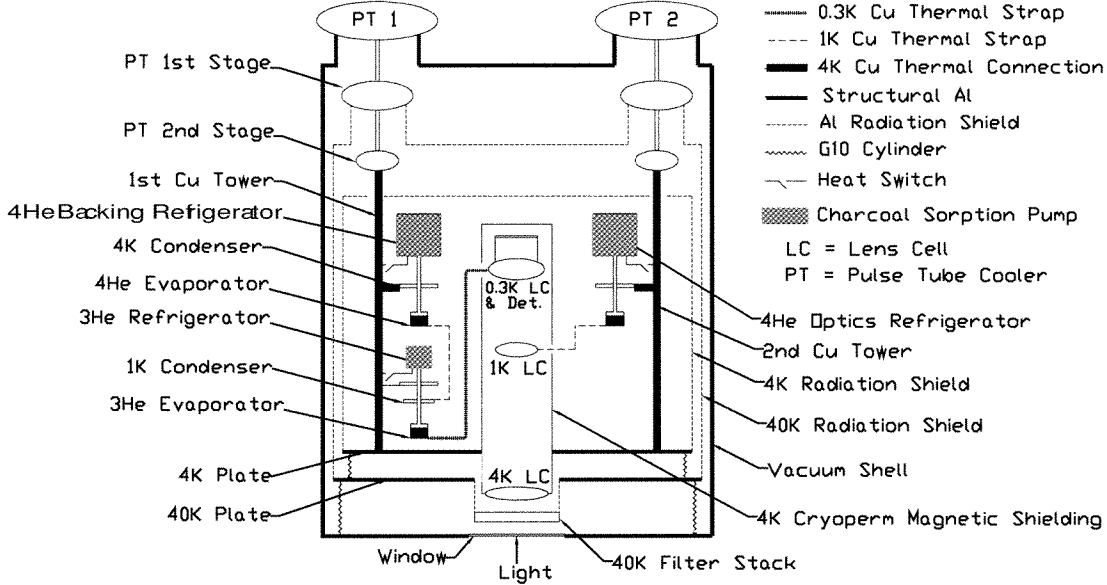[12] Model PT-410 cryorefrigerator from Cryomech. For more information see www.cryomech.com.

FIG. 7.— Schematic of the radiation shielding and thermal connections in MBAC. Only a single optics tube is shown, depicting the 148 and 218 GHz channels. The 277 GHz 1 K optics (not shown) are connected to and cooled by the ^{4}He backing refrigerator.

thick and serves as the optical bench to which all of the cold optics are ultimately mounted. The front plate is also an integral part of the mounting of MBAC to ACT. This design allows all of the cold optics to be rigidly mounted to the telescope without relying on the rigidity of the cylindrical cryostat vacuum vessel.

Two additional aluminum plates are attached to the front plate via G-10 cylinders. The first plate ("40K plate") is cooled to $\sim$ 40 K. The second plate ("4K plate"), suspended from the 40 K plate by G-10, is cooled to $\sim$ 4 K. A large radiation shield is attached to each plate. The shields are nested so that the outer 40 K shield completely surrounds the inner one 4 K shield. The helium refrigerators and optics tubes are rigidly mounted to the 4 K plate and are located between the 4 K plate and its corresponding radiation shield.

The vacuum shell is split about 200 mm back from the front plate. Removing the back section of the cryostat decouples and removes the pulse-tube refrigerators from the optics and adsorption refrigerators, allowing easy access to the cold plates, optics, and detectors. All of the cabling for the thermometry, detectors, and the detector readout comes in through ports in the front vacuum shell section. These cables are heat sunk at both the 40K and at 4K plates. An advantage of this design is that it allows for access to all of the cabling, optics, and detectors without making or breaking any cable attachments.

3.9. Optical Support Structures

To minimize weight, aluminum was generally used to mount optical elements at 300 K, 40 K, and 4 K. For the 1 K and 300 mK assemblies, where conductivity is critical and where aluminum is superconducting (resulting in greatly reduced thermal conductivity), oxygen-free high-conductivity copper (OFHC) was generally used. Another reason for using mostly copper below $\approx$ 1 K is potential problems with trapped magnetic flux in superconducting aluminum alloys.

Each optics tube has a compound wedge at its 4 K

base that holds it at the proper angle with respect to the telescope beam. The tubes can be removed individually, which allowed the 148 GHz optics tube to be deployed in MBAC for the 2007 season while the 218 and 277 GHz optics tubes were being constructed.

The second lens and cold stop for each optics tube is held at 1 K. To reduce the load on our ^{4}He refrigerator, we use two concentric and re-entrant G-10 (fiberglass) tubes to connect the 4 K optics to the 1 K optics.

As mentioned in Section 3.1, the third lens/bandpass and the detector package were designed to be a single mechanical unit (magenta in Figure 8). This OFHC unit is suspended from the 1 K optics stack via a Kevlar suspension (not shown in figure). The limited cooling capacity at 300 mK ($\sim$ 5.8 J) and desired hold time of > 18 hours means the total loading from all three frequencies must be less than 80 μW, preventing G-10 from being used here. The 300 mK assembly is enclosed in a light-tight copper shell which shields the detector from 4 K radiation from the surrounding magnetic shielding. The total mass of the 300 mK assembly for each array is approximately 5 kg.

3.10. Mechanical Alignment of MBAC to ACT

MBAC is mounted to ACT at the flange that joins the front plate to the vacuum cylinder, providing an extremely rigid plane that can be precisely aligned with the optical axis of the telescope. This plane was used as the base for all optical elements inside MBAC, ensuring that the alignment was independent of variations in the cylindrical vacuum shell caused by pressure and temperature. Adjustments permit fine tuning MBAC's position before it is bolted in place.

Figure 2 shows the mating of MBAC in the receiver cabin. The width of the receiver cabin is 3.3 meters. The MBAC enters though doors on the front of the receiver cabin (left side of Figure 2), and passes through the MBAC mounting structure whose width is $\approx$ 1 meter, where it is then hoisted and bolted into place. Once
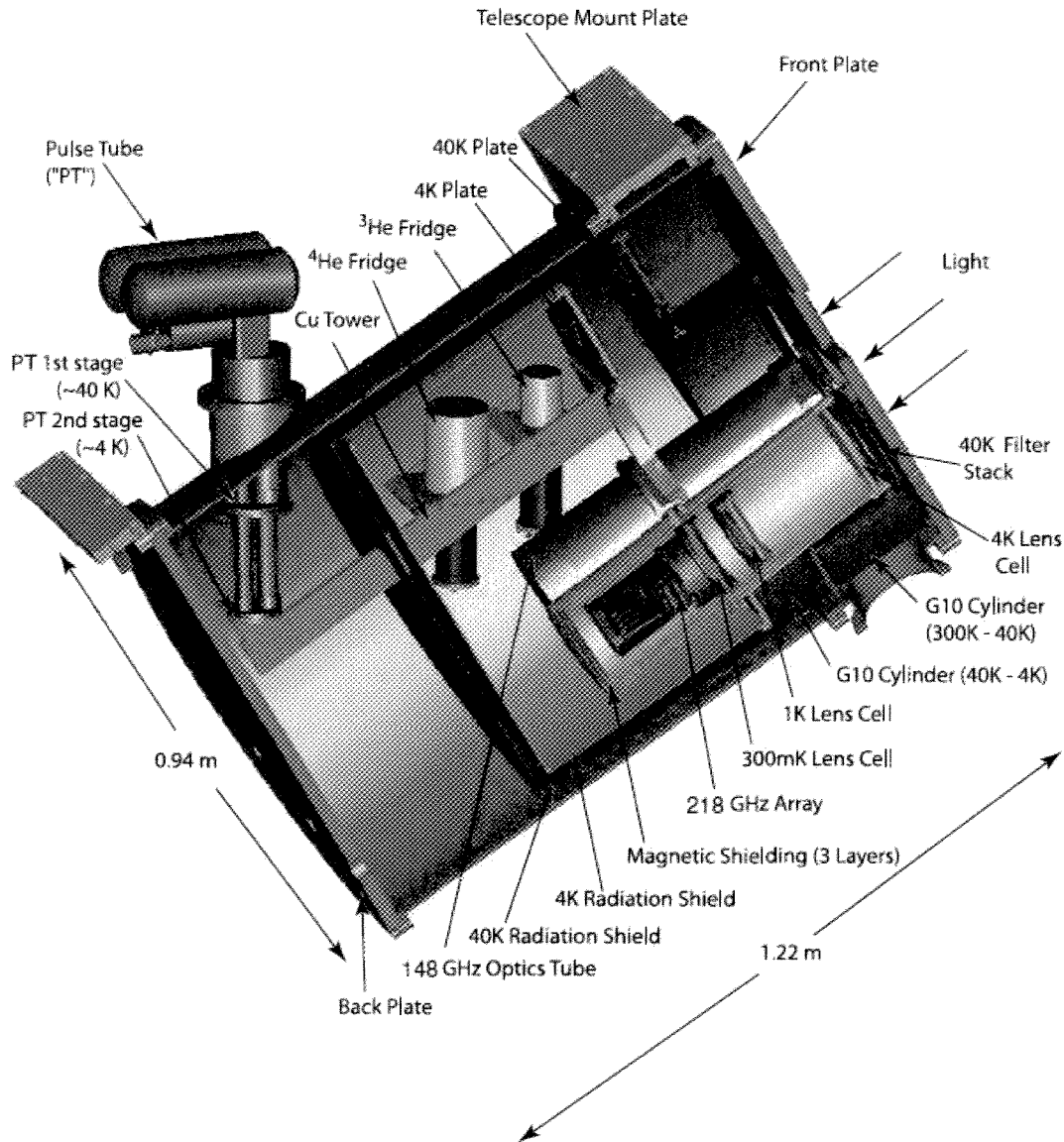
FIG. 8.— Cut away view of the MBAC cryostat showing the location of the internal components. A cut away view of the 218 GHz optics tube is also shown, giving the location of its lenses, filters, and array, which is similar for all three tubes. The 277 GHz optics tube mounts just above the 148 and 218 GHz optics tubes, but is removed for clarity. The connection of the first stage of the pulse tube and its radiation shielding to the 40 K plate is also omitted for clarity.

the cryostat is bolted into the telescope receiver cabin, the laser tracker (Section 2.5) is used to locate the front plate in relation to the primary mirror.

4. DATA ACQUISITION

4.1. Overview

The science data are all written to hard drives on a local acquisition computer (one for housekeeping and three for the science cameras). On each machine, a server broadcasts the data to a central merger computer which aligns and writes the science data from the three cameras, telescope and housekeeping systems to a disk at the telescope site. Large capacity hard drives are problematic at the ACT site due to the dusty environment and low

atmospheric pressure. Therefore all of the site drives are contained in individually pressurized boxes with either ESATA or USB interfaces. Because of limited storage space at the site, these merged data are transmitted to a larger, intermediate, RAID storage node in San Pedro de Atacama with 6.5 TB of available storage. The RAID drives located in San Pedro do not need to be pressurized. The data can also be served to clients on real-time data visualization computers either at the site or the ground station.[13]

To make the large data volume more manageable, we

_____

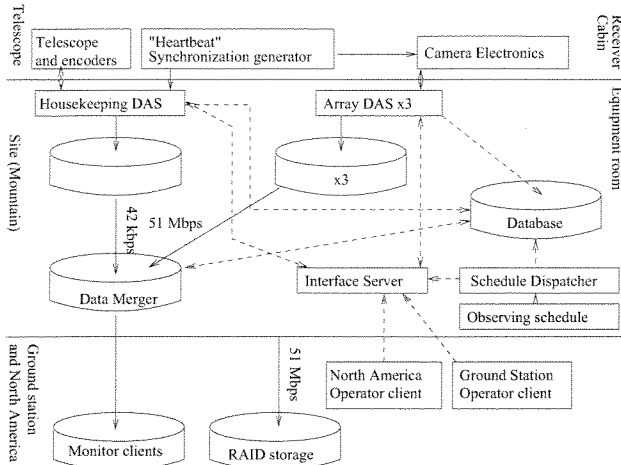[13] Data are displayed in real time using kst (http://kst.kde.org/).

FIG. 9.— Overview of the ACT data and control systems, split into telescope (top), on-site (middle), ground station, and North American systems (bottom). Solid lines show data streams while dashed lines show commanding and file information channels. Cylinders represent data storage. We show only one of three detector array acquisition systems ("Array DAS") for simplicity. The ground station RAID array aggregates data from several machines at the site, so we do not show it as being connected to a particular node. To prepare a transport disk with data to ship back to North America, an operator connects the drive to the RAID array, and the data are automatically copied over based on information in the file database. Operators define a schedule each night and upload it to the schedule dispatcher at the site. Here we have only shown a monitor client in the ground station, but the site also has a system monitor terminal.

compress the data using a fast, lossless algorithm separately to each channel.[14] The compression reduces a typical data file to one-third its original size. The average (compressed) data rate is 80 GB per night. The data are copied from the intermediate RAID storage to external transport disks which are hand-carried on flights to North America. Both the housekeeping and camera data have associated entries in a file database which is periodically checked to automatically move data from the site computers to the ground station, onto transport disks, and to confirm that the data have been properly received (using an md5 checksum) in North America before deleting the data from site computers. There is an associated webpage where operators can track the volume and type of data acquired in real time.

Observations with ACT are defined through a schedule file that specifies an execution time for a task with given parameters. The schedule is tailored for each observing night and coordinates all aspects of science operation. There is no decision structure in the scheduler itself because of the simplicity of the scan strategy. Figure 9 gives a schematic of the acquisition and commanding system.

4.2. Timing

Relative timing to align the camera data, housekeeping and encoders is determined by a system-wide trigger and associated serial stamp. An identical stamp and trigger are passed to each science camera's acquisition electronics through a fiber optic, and to the housekeeping computer (in the equipment room) through an RS485 chan-

nel in the telescope's cable wrap. The system-wide clock rate is defined by counting down a 25 MHz clock over 50 cycles per detector row, over 32 rows of detectors plus one row of dark SQUIDs for the array readout, over 38 array reads per sample trigger. This gives the final rate of $\sim$ 399 Hz. The beam-crossing time of a point source in the scan direction is $\sim$ 10 ms, while in the Earth drift direction it is several seconds. Thus, the $\sim$ 399 Hz fully samples the beam. A Meinberg GPS-169 PCI card disciplines the system clock of the housekeeping computer, with a precision of < 1 ms to GPS time, sufficient for astrometry and book-keeping. Relative timing of encoders and camera data of 5 μs is achieved.

The synchronization serial stamp from the RS485 channel is incorporated into the housekeeping data (including the encoders) through the following chain: 1) in the housekeeping computer, a PCI card receives a 5 MHz biphase signal which encodes serial data stamps at 399 Hz over RS485 from the synchronization box; 2) these trigger CPU interrupts at 399 Hz; 3) a timing driver handles these interrupts by polling the encoders at 399 Hz; 4) the PCI card clocks down the serial stamps to 99.7 Hz, which it uses to poll the housekeeping acquisition electronics; 5) the housekeeping software then assembles the housekeeping and encoder time streams, matching serial stamps; 6) these are written to disk in a flat file format, where for every data frame there are, for example, four times as many 399 Hz encoder values as there are 99.7 Hz housekeeping data frames. The camera, encoder, and housekeeping data are synchronized and stored in the "dirfile" format, where one file represents each channel. For a complete discussion of the ACT timing see Hincks (2009).

4.3. Housekeeping readout

Housekeeping comprises all electronics and systems other than the camera and its electronics and the telescope motion control. The primary systems within housekeeping are the cryogenic thermal readouts and controllers, the telescope health readouts, the telescope motion encoders, and auxiliary monitors. The telescope's azimuth and elevation encoder signals are read by a Heidenhain (model IK220) PCI card in the housekeeping computer over RS485 from the cable wrap. Cryogenic housekeeping is read at 99.7 Hz and auxiliary channels (such as the mirror temperature) are read from 1 − 20 Hz asynchronously by a Sensoray 2600 DAQ. Weather data are available from an on-site WeatherHawk station and from the APEX collaboration.[15]

5. BEAMS

Observations of planets were used to determine the positions of detectors in the focal plane (Swetz 2009), to calibrate detector response, and to measure beam profiles for the determination of the window function (Hincks et al. 2009). Detector position and beam shape measurements relied especially on observations of Saturn.

Observations of Saturn were made approximately every second night during the 2008 season as the planet rose or set through the ACT observing elevation of 50°.5. The planet observations were accomplished using the same fixed-elevation scan strategy and scan speed as the ACT survey data.

---

[14] The compression code slim is publicly available at http://slimdata.sourceforge.net/.

[15] http://www.apex-telescope.org/weather/index.html.

The maps are shown in Figure 10. Maximum likelihood maps were made of each Saturn observation following the method described in Fowler et al. (2010), but with a less sophisticated approach to the removal of low-frequency atmospheric noise. For each map, the detector noise spectra were estimated from the data after fitting and removing a single common mode. The solution for each map was found using a conjugate gradient technique, with a low frequency common mode removed between each iteration. Only 5–10 iterations were necessary to provide adequate convergence. The maps are made in tangent plane coordinates, centered at the expected planet peak position, with the x-axis parallel to the scanning direction.

The beam maps in Figure 10 are the result of co-adding 23, 30, and 13 individual Saturn maps for 148 GHz, 218 GHz, and 277 GHz, respectively. (The lower yield of high quality maps in 277 GHz is due to relative gain drifts in some detectors.) Small, variable offsets in the planet position relative to the center of each map were removed prior to combining the maps.

Point-spread function quality was assessed by measuring the solid angle and FWHM of the beam maps in each array. The results are summarized in Table 6 and the solid angles are consistent with those presented in Hincks et al. (2009) which used a different map-making method and data subset. An elliptical Gaussian is fitted to the peak of the beam profile. The axis angle is the angle of the semi-major axis relative to the x-axis, increasing counter-clockwise.

TABLE 6
SUMMARY OF BEAM PARAMETERS

	148 GHz	218 GHz	277 GHz
Solid Angle[a] (nsr)	217.7 ± 3.6	117.6 ± 2.8	97 ± 12
Major FWHM[a] (′)	1.401 ± 0.003	1.012 ± 0.001	0.891 ± 0.04
Minor FWHM[a] (′)	1.336 ± 0.001	0.991 ± 0.001	0.858 ± 0.005
Axis Angle[a] (°)	66 ± 1	45 ± 2	66 ± 10

[a]The error bars are effective 1-σ errors. The relatively large size of the 277 GHz error bar is due to the systematic errors from atmospheric modeling and is expected to improve.

The beam shapes are consistent with an Airy pattern integrated over the frequency band-width of the filters and non-zero extent of the detectors. First side lobe peaks are apparent at approximately the −15 dB level, at radii of roughly 1.7′, 1.2′ and 1.0′. A simple model of the optics predicts beam FWHM of 1.38′, 1.03′ and 0.88′ for the three arrays (Niemack 2008). This model was calculated for a single detector near the middle of the array and assumes uniform primary illumination, a circular aperture, and takes into account the non-point-like extent of the detectors. It does not include diffraction analysis or integration of beam variation across the array, while the planet measurements are an average across all detectors in each array. Despite the simplifications, the measured FWHM are consistent with the model.
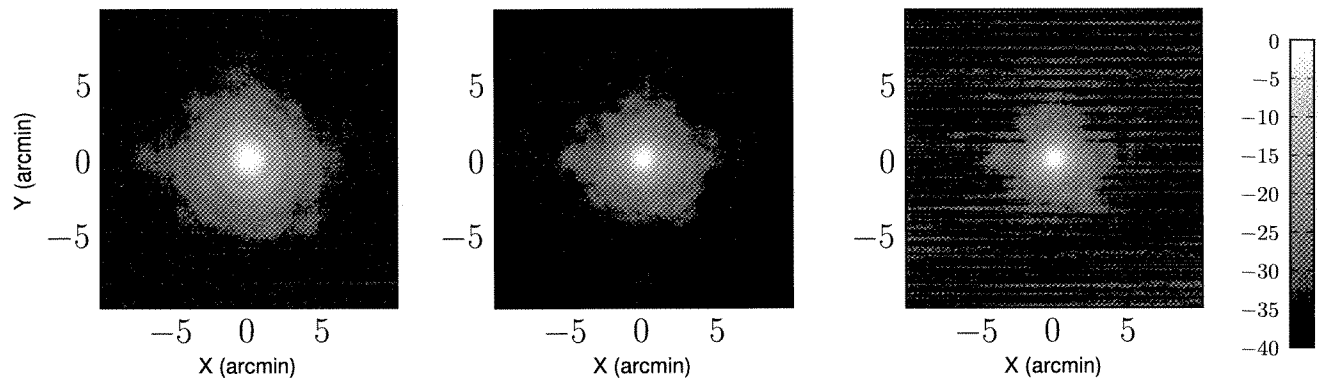
FIG. 10.— Beam maps for the 148 GHz, 218 GHz and 277 GHz arrays (from left to right), made from 23, 30, and 13 (respectively) observations of Saturn.

REFERENCES

Asad M. Aboobaker. *A new millimeter-wave camera for CMB observations.* PhD thesis, Princeton University, 2006.

P. A. R. Ade, G. Pisano, C. Tucker, and S. Weaver. A review of metal mesh filters. In Jonas Zmuidzinas, Wayne S. Holland, Stafford Withington, and William D. Duncan, editors, *Proc. SPIE*, volume 6275, page 62750T, July 2006.

E. S. Battistelli, M. Amiri, B. Burger, M. J. Devlin, S. R. Dicker, W. B. Doriese, R. Dünner, R. P. Fisher, J. W. Fowler, M. Halpern, M. Hasselfield, G. C. Hilton, A. D. Hincks, K. D. Irwin, M. Kaul, J. Klein, S. Knotek, J. M. Lau, M. Limon, T. A. Marriage, M. D. Niemack, L. Page, C. D. Reintsema, S. T. Staggs, D. S. Swetz, E. R. Switzer, R. J. Thornton, and Y. Zhao. Automated SQUID tuning procedure for kilo-pixel arrays of TES bolometers on the Atacama Cosmology Telescope. In William D. Duncan, Wayne S. Holland, Stafford Withington, and Jonas Zmuidzinas, editors, *Proc. SPIE*, volume 7020, page 702028. SPIE, 2008.

D. J. Benford, G. M. Voellmer, J. A. Chervenak, K. D. Irwin, H. S. Moseley, R. A. Shafer, J. G. Staguhn, and G. J. Stacey. Design and Fabrication of Two-Dimensional Superconducting Bolometer Arrays. In T. G. Phillips & J. Zmuidzinas, editor, *Society of Photo-Optical Instrumentation Engineers (SPIE) Conference Series*, volume 4855 of *Society of Photo-Optical Instrumentation Engineers (SPIE) Conference Series*, pages 552–562, February 2003.

M. L. Brown, P. Ade, J. Bock, M. Bowden, G. Cahill, P. G. Castro, S. Church, T. Culverhouse, R. B. Friedman, K. Ganga, W. K. Gear, S. Gupta, J. Hinderks, J. Kovac, A. E. Lange, E. Leitch, S. J. Melhuish, Y. Memari, J. A. Murphy, A. Orlando, C. O'Sullivan, L. Piccirillo, C. Pryke, N. Rajguru, B. Rusholme, R. Schwarz, A. N. Taylor, K. L. Thompson, A. H. Turner, E. Y. S. Wu, M. Zemcov, and The QUaD collaboration. Improved Measurements of the Temperature and Polarization of the Cosmic Microwave Background from QUaD. *ApJ*, 705:978–999, November 2009.

J. A. Chervenak, K. D. Irwin, E. N. Grossman, John M. Martinis, C. D. Reintsema, and M. E. Huber. Superconducting multiplexer for arrays of transition edge sensors. *Applied Physics Letters*, 74(26):4043–4045, 1999.

H. C. Chiang, P. A. R. Ade, D. Barkats, J. O. Battle, E. M. Bierman, J. J. Bock, C. D. Dowell, L. Duband, E. F. Hivon, W. L. Holzapfel, V. V. Hristov, W. C. Jones, B. G. Keating, J. M. Kovac, C. L. Kuo, A. E. Lange, E. M. Leitch, P. V. Mason, T. Matsumura, H. T. Nguyen, N. Ponthieu, C. Pryke, S. Richter, G. Rocha, C. Sheehy, Y. D. Takahashi, J. E. Tolan, and K. W. Yoon. Measurement of CMB Polarization Power Spectra from Two Years of BICEP Data. *arXiv:0906.1181*, June 2009.

L. Danese and R.B. Partridge. Atmospheric emission models: confrontation between observational data and predictions in the 2.5-300 GHz frequency range. *Astrophysical Journal*, 342(1):604 – 15, 1989.

M.J. Devlin, S.R. Dicker, J. Klein, and M.P. Supanich. A high capacity completely closed-cycle 250 mk 3He refrigeration system based on a pulse tube cooler. *Cryogenics*, 44:611–616, 2004.

S.R. Dicker, P. M. Korngut, B. S. Mason, P. A. R. Ade, J. Aguirre, T. J. Ames, D. J. Benford, T. C. Chen, J. A. Chervenak, W. D. Cotton, M. J. Devlin, E. Figueroa-Feliciano, K. D. Irwin, S. Maher, M. Mello, S. H. Moseley, D. J. Tally, C. Tucker, and S. D. White. MUSTANG: 90 GHz science with the Green Bank Telescope. In William D. Duncan, Wayne S. Holland, Stafford Withington, and Jonas Zmuidzinas, editors, *Proc. SPIE*, volume 7020. SPIE, 2008.

J. W. Fowler, V. Acquaviva, P. A. R. Ade, P. Aguirre, M. Amiri, J. W. Appel, L. F. Barrientos, E. S. Battistelli, J. R. Bond, B. Brown, B. Burger, J. Chervenak, S. Das, M. J. Devlin, S. R. Dicker, W. B. Doriese, J. Dunkley, R. Dünner, T. Essinger-Hileman, R. P. Fisher, A. Hajian, M. Halpern, M. Hasselfield, C. Hernández-Monteagudo, G. C. Hilton, M. Hilton, A. D. Hincks, R. Hlozek, K. M. Huffenberger, D. H. Hughes, J. P. Hughes, L. Infante, K. D. Irwin, R. Jimenez, J. B. Juin, M. Kaul, J. Klein, A. Kosowsky, J. M. Lau, M. Limon, Y. -. Lin, R. H. Lupton, T. A. Marriage, D. Marsden, K. Martocci, P. Mauskopf, F. Menanteau, K. Moodley, H. Moseley, C. B. Netterfield, M. D. Niemack, M. R. Nolta, L. A. Page, L. Parker, B. Partridge, H. Quintana, B. Reid, N. Sehgal, J. Sievers, D. N. Spergel, S. T. Staggs, D. S. Swetz, E. R. Switzer, R. Thornton, H. Trac, C. Tucker, L. Verde, R. Warne, G. Wilson, E. Wollack, and Y. Zhao. The Atacama Cosmology Telescope: A Measurement of the 600 < ℓ < 8000 Cosmic Microwave Background Power Spectrum at 148 GHz. *ArXiv e-prints*, January 2010.

J. W. Fowler, W. B. Doriese, T. A. Marriage, H. T. Tran, A. M. Aboobaker, C. Dumont, M. Halpern, Z. D. Kermish, Y.-S. Loh, L. A. Page, S. T. Staggs, and D. H. Wesley. Cosmic Microwave Background Observations with a Compact Heterogeneous 150 GHz Interferometer in Chile. *ApJS*, 156:1–11, January 2005.

J. W. Fowler, M. D. Niemack, S. R. Dicker, A. M. Aboobaker, P. A. R. Ade, E. S. Battistelli, M. J. Devlin, R. P. Fisher, M. Halpern, P. C. Hargrave, A. D. Hincks, M. Kaul, J. Klein, J. M. Lau, M. Limon, T. A. Marriage, P. D. Mauskopf, L. Page, S. T. Staggs, D. S. Swetz, E. R. Switzer, R. J. Thornton, and C. E. Tucker. Optical design of the Atacama Cosmology Telescope and the Millimeter Bolometric Array Camera. *Appl. Opt.*, 46(17):3444–3454, 2007.

A. D. Hincks, V. Acquaviva, P. Ade, P. Aguirre, M. Amiri, J. W. Appel, L. F. Barrientos, E. S. Battistelli, J. R. Bond, B. Brown, B. Burger, J. Chervenak, S. Das, M. J. Devlin, S. Dicker, W. B. Doriese, J. Dunkley, R. Dünner, T. Essinger-Hileman, R. P. Fisher, J. W. Fowler, A. Hajian, M. Halpern, M. Hasselfield, C. Hernández-Monteagudo, G. C. Hilton, M. Hilton, R. Hlozek, K. Huffenberger, D. Hughes, J. P. Hughes, L. Infante, K. D. Irwin, R. Jimenez, J. B. Juin, M. Kaul, J. Klein, A. Kosowsky, J. M. Lau, M. Limon, Y. -. Lin, R. H. Lupton, T. Marriage, D. Marsden, K. Martocci, P. Mauskopf, F. Menanteau, K. Moodley, H. Moseley, C. B. Netterfield, M. D. Niemack, M. R. Nolta, L. A. Page, L. Parker, B. Partridge, H. Quintana, B. Reid, N. Sehgal, J. Sievers, D. N. Spergel, S. T. Staggs, O. Stryzak, D. Swetz, E. Switzer, R. Thornton, H. Trac, C. Tucker, L. Verde, R. Warne, G. Wilson, E. Wollack, and Y. Zhao. The Atacama Cosmology Telescope (ACT): Beam Profiles and First SZ Cluster Maps. *arXiv:0907:0461*, July 2009.

A. D. Hincks, P. A. R. Ade, C. Allen, M. Amiri, J. W. Appel, E. S. Battistelli, B. Burger, J. A. Chervenak, A. J. Dahlen, S. Denny, M. J. Devlin, S. R. Dicker, W. B. Doriese, R. Dünner, T. Essinger-Hileman, R. P. Fisher, J. W. Fowler, M. Halpern, P. C. Hargrave, M. Hasselfield, G. C. Hilton, K. D. Irwin, N. Jarosik, M. Kaul, J. Klein, J. M. Lau, M. Limon, R. H. Lupton, T. A. Marriage, K. L. Martocci, P. Mauskopf, S. H. Moseley, C. B. Netterfield, M. D. Niemack, M. R. Nolta, L. Page, L. P. Parker, A. J. Sederberg, S. T. Staggs, O. Stryzak, D. S. Swetz, E. R. Switzer, R. J. Thornton, C. Tucker, E. J. Wollack, and Y. Zhao. The effects of the mechanical performance and alignment of the Atacama Cosmology Telescope on the sensitivity of microwave observations. In William D. Duncan, Wayne S. Holland, Stafford Withington, and Jonas Zmuidzinas, editors, *Proc. SPIE*, volume 7020, page 70201P. SPIE, 2008.

Adam D. Hincks. *Towards a Mass-Limited Catalog of Galaxy Clusters from the Atacama Cosmology Telescope.* PhD thesis, Princeton University, 2009.

E. Komatsu, J. Dunkley, M. R. Nolta, C. L. Bennett, B. Gold, G. Hinshaw, N. Jarosik, D. Larson, M. Limon, L. Page, D. N. Spergel, M. Halpern, R. S. Hill, A. Kogut, S. S. Meyer, G. S. Tucker, J. L. Weiland, E. Wollack, and E. L. Wright. Five-Year Wilkinson Microwave Anisotropy Probe (WMAP) Observations: Cosmological Interpretation. *ApJS*, 180:330–376, February 2009.

J.W. Lamb. Miscellaneous data on materials for millimetre and submillimetre optics. *International Journal of Infrared and Millimeter Waves*, 17(12):1997–2034, 1996.

J. Lau, J. Fowler, T. Marriage, L. Page, J. Leong, E. Wishnow, R. Henry, E. Wollack, M. Halpern, D. Marsden, and G. Marsden. Millimeter-wave antireflection coating for cryogenic silicon lenses. *Appl. Opt.*, 45:3746–3751, June 2006.

Judy M. Lau. *CCAM: A Novel Millimeter-Wave Instrument Using A Close-Packed TES Bolometer Array.* PhD thesis, Princeton University, 2008.

Mary J. Li, Christine A. Allen, Scott A. Gordon, Jonathan L. Kuhn, David B. Mott, Caroline K. Stahle, and Liqin L. Wang. Fabrication of pop-up detector arrays on si wafers. volume 3874, pages 422–431. SPIE, 1999.

T. A. Marriage, J. A. Chervenak, and W. B. Doriese. Testing and assembly of the detectors for the Millimeter Bolometric Array Camera on ACT. *Nuc Inst & Meth. in Phys Res A*, 559:551–553, 2006.

A. Miller, J. Beach, S. Bradley, R. Caldwell, H. Chapman, M. J. Devlin, W. B. Dorwart, T. Herbig, D. Jones, G. Monnelly, C. B. Netterfield, M. Nolta, L. A. Page, J. Puchalla, T. Robertson, E. Torbet, H. T. Tran, and W. E. Vinje. The QMAP and MAT/TOCO Experiments for Measuring Anisotropy in the Cosmic Microwave Background. *ApJS*, 140:115–141, June 2002.

M. D. Niemack, Y. Zhao, E. Wollack, R. Thornton, E. R. Switzer, D. S. Swetz, S. T. Staggs, L. Page, O. Stryzak, H. Moseley, T. A. Marriage, M. Limon, J. M. Lau, J. Klein, M. Kaul, N. Jarosik, K. D. Irwin, A. D. Hincks, G. C. Hilton, M. Halpern, J. W. Fowler, R. P. Fisher, R. Dünner, W. B. Doriese, S. R. Dicker, M. J. Devlin, J. Chervenak, B. Burger, E. S. Battistelli, J. Appel, M. Amiri, C. Allen, and A. M. Aboobaker. A kilopixel array of TES bolometers for ACT: Development, testing, and first light. *J. Low Temp. Phys.*, 151(3-4):690–696, 2008.

Michael D. Niemack. *Towards Dark Energy: Design, Development, and Preliminary Data from ACT.* PhD thesis, Princeton University, 2008.

L. Page, C. Jackson, C. Barnes, C. Bennett, M. Halpern, G. Hinshaw, N. Jarosik, A. Kogut, M. Limon, S. S. Meyer, D. N. Spergel, G. S. Tucker, D. T. Wilkinson, E. Wollack, and E. L. Wright. The Optical Design and Characterization of the Microwave Anisotropy Probe. *ApJ*, 585:566–586, March 2003.

J. R. Pardo, J. Cernicharo, and E. Serabyn. Atmospheric transmission at microwaves (ATM): an improved model for millimeter/submillimeter applications. *IEEE Transactions on Antennas and Propagation*, 49:1683–1694, December 2001.

J. Ruze. Antenna tolerance theory – a review. *Proc. IEEE*, 54:633–640, 1966.

J. L. Sievers, B. S. Mason, L. Weintraub, C. Achermann, P. Altamirano, J. R. Bond, L. Bronfman, R. Bustos, C. Contaldi, C. Dickinson, M. E. Jones, J. May, S. T. Myers, N. Oyarce, S. Padin, T. J. Pearson, M. Pospieszalski, A. C. S. Readhead, R. Reeves, M. C. Shepherd, A. C. Taylor, and S. Torres. Cosmological Results from Five Years of 30 GHz CMB Intensity Measurements with the Cosmic Background Imager. *arXiv:0901.4540*, January 2009.

D. S. Swetz, P. A. R. Ade, C. Allen, M. Amiri, J. W. Appel, E. S. Battistelli, B. Burger, J. A. Chervenak, A. J. Dahlen, S. Das, S. Denny, M. J. Devlin, S. R. Dicker, W. B. Doriese, R. Dünner, T. Essinger-Hileman, R. P. Fisher, J. W. Fowler, X. Gao, A. Hajian, M. Halpern, P. C. Hargrave, M. Hasselfield, G. C. Hilton, A. D. Hincks, K. D. Irwin, N. Jarosik, M. Kaul, J. Klein, S. Knotek, J. M. Lau, M. Limon, R. H. Lupton, T. A. Marriage, K. L. Martocci, P. Mauskopf, S. H. Moseley, C. B. Netterfield, M. D. Niemack, M. R. Nolta, L. Page, L. P. Parker, B. A. Reid, C. D. Reintsema, A. J. Sederberg, N. Sehgal, J. L. Sievers, D. N. Spergel, S. T. Staggs, O. R. Stryzak, E. R. Switzer, R. J. Thornton, C. Tucker, E. J. Wollack, and Y. Zhao. Instrument design and characterization of the Millimeter Bolometer Array Camera on the Atacama Cosmology Telescope. In William D. Duncan, Wayne S. Holland, Stafford Withington, and Jonas Zmuidzinas, editors, *Proc. SPIE*, volume 7020, page 702008. SPIE, 2008.

Daniel S. Swetz. *The Atacama Cosmology Telescope.* PhD thesis, The University of Pennsylvania, 2009.

E. R. Switzer, C. Allen, M. Amiri, J. W. Appel, E. S. Battistelli, B. Burger, J. A. Chervenak, A. J. Dahlen, S. Das, M. J. Devlin, S. R. Dicker, W. B. Doriese, R. Dünner, T. Essinger-Hileman, X. Gao, M. Halpern, M. Hasselfield, G. C. Hilton, A. D. Hincks, K. D. Irwin, S. Knotek, R. P. Fisher, J. W. Fowler, N. Jarosik, M. Kaul, J. Klein, J. M. Lau, M. Limon, R. H. Lupton, T. A. Marriage, K. L. Martocci, S. H. Moseley, C. B. Netterfield, M. D. Niemack, M. R. Nolta, L. Page, L. P. Parker, B. A. Reid, C. D. Reintsema, A. J. Sederberg, J. L. Sievers, D. N. Spergel, S. T. Staggs, O. R. Stryzak, D. S. Swetz, R. J. Thornton, E. J. Wollack, and Y. Zhao. Systems and control software for the atacama cosmology telescope. In Alan Bridger and Nicole M. Radziwill, editors, *Proc. SPIE*, volume 7019, page 70192L. SPIE, 2008.

M. Tegmark. CMB mapping experiments: a designer's guide. *Physical Review D*, 56(8):4514 – 29, 1997.

R. J. Thornton, P. A. R. Ade, C. Allen, M. Amiri, J. W. Appel, E. S. Battistelli, B. Burger, J. A. Chervenak, M. J. Devlin, S. R. Dicker, W. B. Doriese, T. Essinger-Hileman, R. P. Fisher, J. W. Fowler, M. Halpern, P. C. Hargrave, M. Hasselfield, G. C. Hilton, A. D. Hincks, K. D. Irwin, N. Jarosik, M. Kaul, J. Klein, J. M. Lau, M. Limon, T. A. Marriage, K. L. Martocci, P. Mauskopf, S. H. Moseley, M. D. Niemack, L. Page, L. P. Parker, J. Reidel, C. D. Reintsema, S. T. Staggs, O. R. Stryzak, D. S. Swetz, E. R. Switzer, C. Tucker, E. J. Wollack, and Y. Zhao. Opto-mechanical design and performance of a compact three-frequency camera for the millimeter bolometer array camera on the atacama cosmology telescope. In William D. Duncan, Wayne S. Holland, Stafford Withington, and Jonas Zmuidzinas, editors, *Proc. SPIE*, volume 7020, page 70201R. SPIE, 2008.

C. E. Tucker and P. A. R. Ade. Thermal filtering for large aperture cryogenic detector arrays. In Jonas Zmuidzinas, Wayne S. Holland, Stafford Withington, and William D. Duncan, editors, *Proc. SPIE*, volume 6275, page 62750U, July 2006.

D. Woody, D. MacDonald, M. Bradford, R. Chamberlin, M. Dragovan, P. Goldsmith, J. Lamb, S. Radford, and J. Zmuidzinas. Panel options for large precision radio telescopes. In *Society of Photo-Optical Instrumentation Engineers (SPIE) Conference Series*, volume 7018 of *Society of Photo-Optical Instrumentation Engineers (SPIE) Conference Series*, July 2008.

E. L. Wright. Scanning and Mapping Strategies for CMB Experiments. *ArXiv Astrophysics e-prints*, November 1996.

Y. Zhao, C. Allen, M. Amiri, J. W. Appel, E. S. Battistelli, B. Burger, J. A. Chervenak, A. Dahlen, S. Denny, M. J. Devlin, S. R. Dicker, W. B. Doriese, R. Dünner, T. Essinger-Hileman, R. P. Fisher, J. W. Fowler, M. Halpern, G. C. Hilton, A. D. Hincks, K. D. Irwin, N. Jarosik, J. Klein, J. M. Lau, T. A. Marriage, K. Martocci, H. Moseley, M. D. Niemack, L. Page, L. P. Parker, A. Sederberg, S. T. Staggs, O. R. Stryzak, D. S.Swetz, E. R. Switzer, R. J. Thornton, and E. J. Wollack. Characterization of transition edge sensors for the millimeter bolometer array camera on the atacama cosmology telescope. In William D. Duncan, Wayne S. Holland, Stafford Withington, and Jonas Zmuidzinas, editors, *Proc. SPIE*, volume 7020, page 70200O. SPIE, 2008.